Journal of Energy and Power Engineering 7 (2013) 1634-1643

Modeling Abrasion Forces in a Pneumatically Powered Grinding Tool Using Compressible Large Eddy Simulation

Kristofer Leach and Rodion Groll

Center of Applied Space Technology and Microgravity, University of Bremen, Bremen 28359, Germany

Received: November 28, 2012 / Accepted: February 19, 2013 / Published: September 30, 2013.

Abstract: This paper describes the design of a new kind of miniature abrading sphere, which is magnetically mounted inside a spherical gap and set in rotation pneumatically with air. Large eddy simulation is performed in conjunction with the compressible Smagorinsky model. Minimal temperature variation allows for the assumption of adiabatic walls. Fluid-solid interaction is modeled using the law of the wall for compressible turbulent flow. A parametric study is done to determine optimal geometric layout while taking physical restrictions into account. The resulting optimal configuration is then examined in detail in order to determine demands to be met by the computerized control of the magnetic bearing as well as to quantify the force available to the abrasion process. Finally, a mathematical relation is given that determines available abrasion force depending on standard volumetric flow rate and rotation frequency. The findings presented here provide a basis for further development of smaller versions of the tool.

Key words: CFD, compressible large eddy simulation, fluid-solid interaction, miniature-grinding tools, OpenFOAM.

1. Introduction

Project GrindBall is an applied research project sponsored by the DFG (German Research Foundation) as part of the work-group SPP 1476 (small machine tools) involving simulation, electro-magnetic control, and manufacture of a miniature abrading device [1]. The workload in this project is hence distributed on to three institutes: computational simulation is conducted at the ZARM (Center of Applied Space Technology and Microgravity), the electro-magnetic control element is developed at the IALB (Institute for Electrical Drives, Power Electronics and Devices), and manufacture of the tool itself is undertaken by the LFM (Laboratory for Precision Machining).

1.1 Motivation

Miniaturization is of great importance in many fields such as mechatronics, optics, or medicine as it enables new functionality or makes processes more economical [2]. While increasing precision has made it possible to produce smaller and smaller workpieces, the tools used to work on them have for the most part remained constant in size. The skewed ratio of tool size to workpiece size creates a growing ecological, economical and technical inefficiency regarding respective processes. Until now, miniaturizing existing tools was performed in order to combat this skewed ratio. This approach is, however, reaching its limits regarding technical feasibility and usefulness. For this reason, new innovative concepts and tools need to be developed in order to advance in the field of miniaturization. Since the ratio of surface to volume increases dramatically with increasing miniaturization, one has, proportionally, far more functional surface to work with as volume decreases. This effect is extremely useful for abrasive tools, as the control dynamics improve with deceasing tool size, thus also

Corresponding author: Rodion Groll, Ph.D., research fields: thermo-fluid dynamics and compressible flow. E-mail: groll@zarm.uni-bremen.de.

improving the tools ability to adapt to particular machining conditions. Most abrasive tools used to create micro cavities suffer from the following problem: since the axis of rotation and its orientation to the workpiece are crucial in ensuring positive grinding results, aligning the axis of rotation is key when grinding a cavity. A grinding pencil, for instance, has its theoretical maximum effectiveness when the axis of rotation is parallel to the work piece. This, however, is not always practical since the grinding pencil's mounting apparatus could touch down on to the workpiece. Furthermore, should the axis of rotation be perpendicular to the workpiece, the grinding pencil's abrasion would tend to zero. This problem can be countered by tilting the apparatus slightly, however, this still delivers mediocre results at best. Fig. 1 depicts the problems stated along with a theoretical solution in which the axis of rotation is parallel to the workpiece at all times, thereby maximizing the tool's effectiveness. It is the goal of project GrindBall to develop such a tool, which, in addition, combines propulsion and control into one single element.

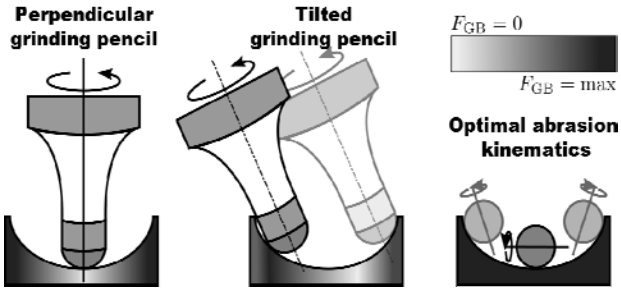

Fig. 1 Abrasion force depending on axis orientation.

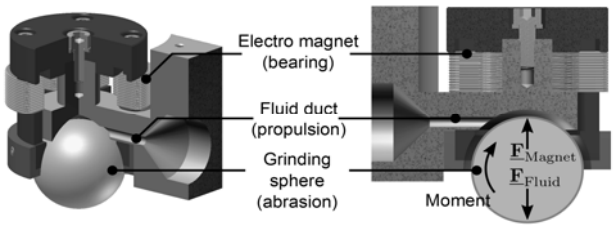

Fig. 2 GrindBall-basic setup.

1.2 Basic Setup

To achieve the objectives stated above, fluid driven propulsion is used in conjunction with a ferro-magnetic sphere covered with an abrasive coating. The repelling force of the fluid is compensated by an adjustable opposing magnetic force, so that the sphere is held in a predefined position relative to the shaft at all times (Fig. 2). A magnetic bearing is used to control the tool by preventing any unwanted movement of the sphere while at the same time defining an axis of rotation in combination with the flow [3].

The first prototype utilizes a sphere with a diameter of 40 mm. Throughout the duration of the project, this diameter is to be gradually scaled down to 1 mm, with surrounding elements shrinking in proportion. The force necessary to achieve abrasion is applied by the fluid flow. Due to the sphere having little mass and the resulting low moment of inertia, high rotational frequencies and an extremely high control dynamic are to be expected. Planning and construction of the GrindBall requires interdisciplinary cooperation between production technology, electrical engineering, and fluid mechanics.

1.3 Goals

This paper begins by introducing the equations governing computational simulations used in the scope of this project. A parametric study is performed to determine optimal configuration of the tool for the case of a 40 mm sphere. Once found, the optimal layout is subjected to a variety of simulations, which ascertain the GrindBall's possibilities and limitations. This includes identifying conditions for stable and efficient operation of the tool, quantification of acting forces, and derivation of a mathematical relation governing the force available to the abrasion process. In addition, the results presented here are intended to serve as a basis for future development of the GrindBall, i.e. step-by-step miniaturization.

2. Simulation Framework

The following introduces the equations and models governing the simulations conducted for the GrindBall.

2.1 Large Eddy Simulation

The basic principle in LES (large eddy simulation) is

to differentiate between resolved scales and subgrid scales. The former are those, which are directly calculated by the governing equations while the latter are included by means of a statistical model. A generic property ψ is split into two separate components:

$$\psi = \overline{\psi} + \psi' \tag{1}$$

where, the overbar denotes a filtered quantity and the prime denotes a fluctuation. Additionally, density-weighted Favre filtering [4] is used for compressible flow:

$$\tilde{\psi} = \frac{\overline{\rho\psi}}{\overline{\rho}} \tag{2}$$

which prevents having to model additional terms. In practice, ψ is unknown and hence can not be filtered. Instead, the filtered quantity $\overline{\psi}$ is taken as a result obtained on a finite computational grid cell. The information ψ', which is lost as it is too fine to be captured by the grid resolution, is subsequently modeled to compensate.

2.2 Transport Equations

The Favre filtered continuity equation is given by:

$$\frac{\partial\overline{\rho}}{\partial t} + \frac{\partial\overline{\rho}\widetilde{u}_i}{\partial x_i} = 0 \tag{3}$$

Conservation of momentum is governed by:

$$\frac{\partial\overline{\rho}\tilde{u}_i}{\partial t} + \frac{\partial\overline{\rho}\tilde{u}_j\tilde{u}_i}{\partial x_i} = -\frac{\partial\overline{p}}{\partial x_i} + 2(\mu+\mu_{sgs})\frac{\partial\tilde{S}_{ij}}{\partial x_j} \tag{4}$$

with:

$$\tilde{S} = \frac{1}{2}\left(\frac{\partial\tilde{u}_i}{\partial x_j} + \frac{\partial\tilde{u}_j}{\partial x_i}\right) - \frac{1}{3}\frac{\partial\tilde{u}_k}{\partial x_k}\delta_{ij} \tag{5}$$

Conservation of energy in terms of enthalpy is given by:

$$\frac{\partial\overline{\rho}\tilde{h}}{\partial t} + \frac{\partial\overline{\rho}\tilde{u}_j\tilde{h}}{\partial x_j} = \frac{D\overline{p}}{Dt} + \frac{\partial}{\partial x_j}\left(\left(\alpha+\alpha_{sgs}\right)\frac{\partial\tilde{h}}{\partial x_j}\right) \tag{6}$$

2.3 Ideal Gas Law

Pressure and density are linked using the ideal gas law (cp. [5]):

$$p = \rho RT \tag{7}$$

2.4 Sutherland's Viscosity Model

The viscosity's temperature dependence is determined using Sutherland's viscosity model stated in Ref. [6]:

$$\mu = \mu_0\left(\frac{T}{T_0}\right)^{\frac{3}{2}}\frac{T_0+T_S}{T+T_S} \tag{8}$$

where, μ_0 = 1.8325 × 10^{-5} kg·m^{-1}s^{-1} is the reference viscosity of air measured at a reference temperature of T_0 = 296.15 K and T_S = 120 K is the Sutherland constant for air.

2.5 Smagorinsky Subgrid Scale Model

Modeling subgrid scale models is done using the compressible Smagorinsky model according to Ref. [7]:

$$\mu_{sgs} = C_k\rho\Delta\sqrt{k_{sgs}} \tag{9}$$

where, k_{sgs} represents the modeled turbulent kinetic energy and C_k = 0.02. Modeled thermal conductivity is proportional to the modeled viscosity:

$$\alpha_{sgs} = \frac{\mu_{sgs}}{\mathrm{Pr}_{sgs}} \tag{10}$$

where, Pr_{sgs} is the subgrid scale Prandtl number, here taken to be 0.9.

2.6 Law of the Wall

The Law of the Wall discussed in Ref. [5] states that the mean velocity at a given point in a turbulent flow is proportional to the logarithm of the distance between the point in question and the nearest wall or boundary layer:

$$u^* = \frac{1}{\kappa}\ln\left(y^*\right) + C \tag{11}$$

where, $u^* = u/u_\tau$ is a dimensionless velocity, $u_\tau = \sqrt{\tau_w/\rho}$ is the shear velocity and τ_w is the wall shear stress. Furthermore, $y^* = yu_\tau/\nu$ is a dimensionless distance from the wall where y is the actual wall distance, made dimensionless by u_τ and the kinematic viscosity ν. C is a constant of

integration and κ is the Von Kármán constant equal to 0.41. This holds for $y^* \geq 30$. Adjacent to the wall, i.e., for $y^* \leq 5$, the velocity is given by $u^* = y^*$. For $5 < y^* < 30$, the law relies on an approximation that smoothly combines the two regions.

2.7 Simulation Setup

Two sets of simulations are performed using the pressure-based compressible FVM (finite volume method) solver rhoPimpleFoam which is part of the open source CFD package OpenFOAM-2.0.1. The first is a parametric study which aims to determine the optimum geometric layout of the tool. The second investigates the optimum geometry and attempts to quantify forces acting on the grinding sphere and the force available to the abrasion process. Rough walls are neglected pending an experimental comparison between smooth and coated grinding spheres.

2.8 Computational Grid

Simulations are conducted on a single mesh consisting of approximate 1 million cells for the parametric study and on two meshes (one coarse with approximate 1.8 million cells and one fine with approximate 5 million cells) for the analysis of the optimal geometry. The reason for conducting the second part on two meshes is to save computational cost while still achieving accurate results. The computation is first run on a coarse mesh until equilibrium is reached. The results are then mapped on to the finer grid where the simulation is continued. The fine mesh is based on the coarse mesh, but with each cell inside the spherical gap refined once in each direction, thus increasing the number of cells inside the gap by a factor of 8. Also note that since the simulations involve turbulence modeling, equilibrium does not refer to a steady state, but fluctuation about a steady mean.

2.9 Discretization Methods

Spatial discretization is performed using the CDS (central differencing scheme) and temporal discretization is done using the Euler method. Both methods are described in Ref. [8]. Furthermore, pressure correction is performed with the PIMPLE method, which is an amalgamation of the SIMPLE and PISO methods also discussed in Ref. [8].

2.10 Boundary Conditions

At the inlet, velocity is calculated based on a given mass flow rate. Pressure adheres to a zero gradient condition. Temperature is set to room temperature at 293.15 K. μ_{sgs} and α_{sgs} are calculated directly based on available data. Boundary conditions at the outlet are zero gradient for flow exiting the system as well as for pressure and temperature. Flow entering the system is at room temperature and obtains its velocity based on mass flow rate. Again, μ_{sgs} and α_{sgs} are calculated directly. Static walls ensure a no-slip condition by enforcing a velocity of zero. Pressure and temperature are set to zero gradient. μ_{sgs} and α_{sgs} are determined using wall functions, which ensure that the law of the wall is applied. The grinding sphere is a special case. As it is rotating, surface velocity is calculated based on a given rotation speed about the axis of rotation. All other variables adhere to the same conditions as for static walls.

2.11 Forces

The main criteria in this analysis are forces and moments acting on the sphere. Pressure p is calculated in each cell adjacent to the sphere and multiplied by the surface normal belonging to the corresponding cell face making up part of the sphere's surface. The sum of the resulting vectors yields the total pressure force acting on the sphere:

$$\underline{F}_p = \sum_{i=1}^{n} p_i \underline{n}_i \tag{12}$$

where, $\underline{n}_i$ is the surface normal vector of the individual sphere boundary face i, and n is the total number of cell faces on the sphere. This is the discrete equivalent of integrating pressure over the entire surface.

Viscous forces are calculated using the part of the stress tensor defined in Eq. (5) that acts on the cell face *i:*

$$\underline{F}_{\mu} = \sum_{i=1}^{n} \underline{n}_i \cdot 2\left[\mu + \mu_{sgs}\right]_i \underline{\underline{\tilde{S}}}_{ij} \qquad (13)$$

Viscous moment is calculated by taking the cross product of the vector $\underline{r}_i$ which points from the center of the sphere to the center of the cell face, with the viscous force:

$$\underline{M}_{\mu} = \sum_{i=1}^{n} \underline{r}_i \times \left(\underline{n}_i \cdot 2\left[\mu + \mu_{sgs}\right]_i \underline{\underline{\tilde{S}}}_{ij} \right) \qquad (14)$$

Henceforth, total forces acting on the sphere, i.e. $\underline{F}_p + \underline{F}_{\mu}$ are referred to as $\underline{F}$ and the force available to the abrasion process is given by:

$$F_{GB} = M_{\mu,y} / r \qquad (15)$$

where, $r = 0.02$ m is the radius of the sphere and $\underline{M}_{p,\mu}$ is the y-component of $\underline{M}_{\mu}$, i.e., the moment acting about the axis of rotation y.

2.12 Time Averaging

Results are averaged over time, beginning from a point at which the simulation has reached equilibrium, according to:

$$\bar{\psi} = \frac{1}{t_n - t_0} \sum_{i=1}^{n-1} \frac{1}{2} \left(\psi_i + \psi_{i+1} \right) \left(t_{i+1} - t_i \right) \qquad (16)$$

where, n is the number of time steps in the interval.

3. Results

The previously discussed principles are now applied to a particular case, namely a pneumatically powered abrading sphere, the GrindBall. First, a parametric study is conducted in order to identify an optimal geometric configuration for the tool. The resulting optimal setup is subsequently simulated and analyzed in detail to determine the demands to be met by the magnetic bearing and the force effectively available to the abrasion process. Furthermore, a mathematical relation governing the behavior of the available abrasion force is derived.

3.1 Parametric Study

The goal of this parametric study is to make the GrindBall as efficient as possible while abiding to certain practical and physical restrictions. The sphere's radius of 40 mm is considered fixed and will not be varied here. Furthermore, air is the only considered medium of pneumatic propulsion.

An important physical restriction is the fact that the height of the spherical gap should not exceed 3 mm, as the resulting heat transfer of the magnetic bearing on to its surroundings would impair prolonged use of the tool. Momentum transfer on to the sphere should be maximized under these conditions while maintaining acceptable pressure forces, which can be easily countered by the magnetic control element. It should furthermore be noted, that the magnetic bearing consists of five individual magnets, four of which exert force on the sphere horizontally and one of which exerts force vertically (Fig. 3).

Hence, the bearing relies on the weight of the sphere itself should the sphere be required to lower its position. The grinding sphere exerts a force approximately equal to 2.5 N in a downward direction due to its own weight. This force should not be overcome by any upward force resulting from effects the flow might have. Mass flow rate at the inlet is chosen such that the mean velocity inside the duct is approximately 230 ms^{-1}. Also, a rotating sphere will not be considered during the parametric study, as it is not a necessary factor when comparing individual geometries.

3.1.1 Variable Parameters

There are essentially three main variable factors considered here. These are the height of the spherical gap h_g in which the abrading sphere is mounted and where most of the momentum transfer on to the sphere takes place, the diameter of the duct h_d which is responsible for introducing the pneumatic propulsion medium into the spherical gap, as well as the offset h_o of the duct relative to the top of the spherical gap. The graphic overview can be seen in Fig. 4. Gap heights of 2 mm, 3 mm, and 4 mm are examined with duct diameters also ranging from 2 mm to 4 mm. Offset is taken to equal to gap height for this first run. Neglecting cases in which duct diameter is less than the

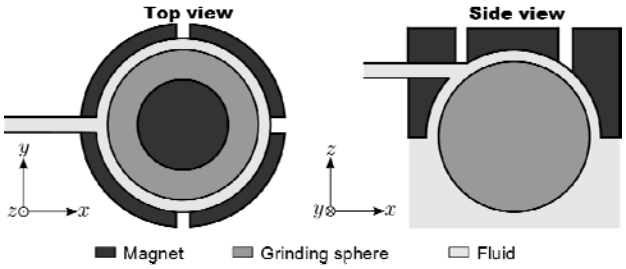

Fig. 3 Magnetic bearing aligned around the grinding sphere.

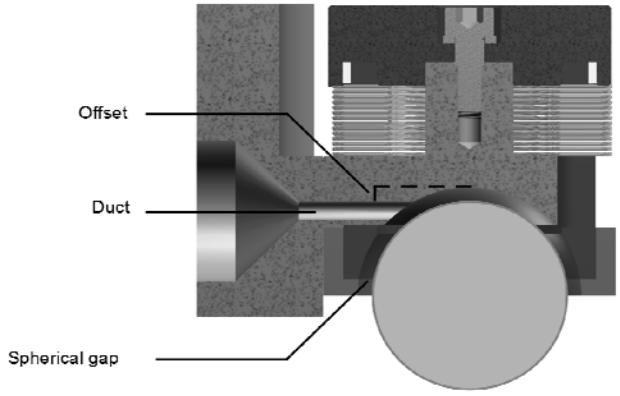

Fig. 4 Variable parameters for the parametric study.

height of the gap results in six individual cases to be considered (Table 1). The 4 mm gap height case is considered here purely as a means of comparison since the maximum practical gap height is 3 mm as stated previously.

Offset of the duct relative to the top of the spherical gap is then examined using the optimum configuration obtained from the first run for the following values: 50%, 75%, 125%, 150%, 175%, and 200%, where the percentage refers to the offset's value relative to gap height.

3.1.2 Simulation Results

The results from the first part of the parametric study can be seen in Fig. 5. Clearly the case with a 2 mm gap and a 4 mm duct delivers the best results in terms of momentum transfer. The 3/4 mm case follows, with 4/4 mm and 2/3 mm closely behind. 3/3 mm and 2/2 mm deliver a rather poor performance by comparison. Forces in x-direction all display a similar average ranging from 0.06 N to 0.13 N. More interesting here are the large differences among standard deviations. From here on, only the top three cases are considered remembering that the 4/4 mm case is not practically

Table 1 Cases considered while examining duct diameter and spherical gap height.

	2 mm duct	3 mm duct	4 mm duct
2 mm gap	¶	¶	¶
3 mm gap		¶	¶
4 mm gap			¶

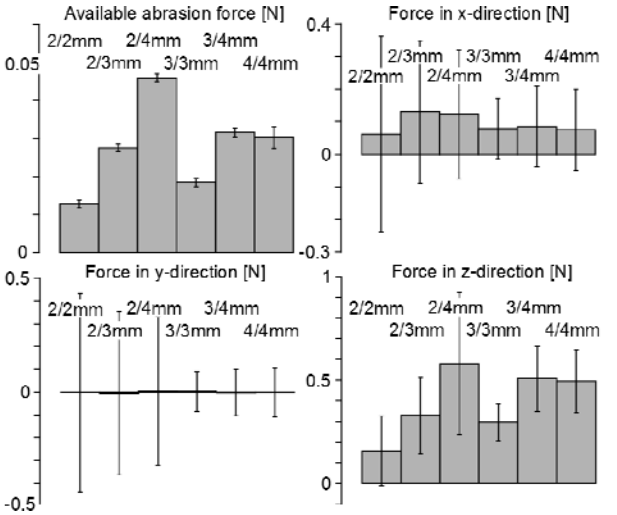

Fig. 5 Results from part one of the parametric study: abrasion force F_{GB} and exerted forces F_x, F_y, and F_z (error bars denote standard deviation).

feasible. The 3/4 mm case's $\sigma(F_x)$ is approximately half of that seen in the cases 2/4 mm and 2/3 mm. This means that the former would deliver much smoother performance as the force exerted does not oscillate as heavily about its mean. Similar observations can be made for F_y and F_z. Forces F_y all display an extremely low average as is to be expected since the geometry is symmetric about $y = 0$ and the main flow direction is perpendicular to the y-axis. Standard deviations again display varying results. Here the cases 2/3 mm and 2/4 mm both deliver a $\sigma(F_y)$ more than three times as large as the 0.1 N seen in the 3/4 mm case. The force F_z is not quite in keeping with F_x and F_y: 2/3 mm delivers the best result with the lowest upward force of $F_z = 0.33$ N and a standard deviation of $\sigma(F_z)$ 3/4 mm and 2/4 mm both show values around 0.5 N for F_z. The standard deviation, however, of 0.34 N for 2/4 mm is more than double the deviation of 0.16 N seen in the 3/4 mm case. Despite having the largest available abrasion force, the 2/4 mm case displays such high standard deviations that make in an impractical choice. The high upward

force F_z combined with a corresponding large standard deviation $\sigma(F_z)$ make this configuration particularly problematic. Comparing 2/3 mm and 3/4 mm sees 3/4 mm as the far better choice. While 2/3 mm shows a lower F_z with similar values for $\sigma(F_z)$, the standard deviations of F_x and F_y are simply too high by comparison. Such highly fluctuating forces could cause strong vibrations, which would in turn cause the magnetic bearing to emit more heat while trying to compensate. This may impair prolonged use of the tool. Generally it can be said that the forces F_{GB}, F_x, and F_z increase with increasing gap height for the cases in which duct diameter is equal to gap height. Furthermore, these forces increase with increasing duct diameter for constant gap height. Standard deviations of F_{GB} show very little difference across all cases. Forces F_x, F_y, and F_z, however, display great variations in their standard deviations. The standard deviations seen for all cases using 2 mm gap height are far greater that those seen using a 3 mm or 4 mm gap. Gap heights of 3 mm and 4 mm are similar regarding $\sigma(\underline{F})$. A smaller gap thus seems to promote heavier vibration of the sphere while a larger gap enables smoother operation. Varying the duct diameter at constant gap height shows similar results for standard deviations in all cases.

The optimum case from the first part of the study with a 3 mm gap height h_g and a 4 mm duct diameter h_d is now subjected to a second study with varying offset. The offset h_o is given as a percentage of h_g and is measured as the vertical distance between the top of the gap and the highest point of the duct (Fig. 4).

Cases investigated are for $h_o \in \{50\%, 75\%, 100\%, 125\%, 150\%, 175\%, 200\%\}$. An offset higher than 200% can not be considered since the hose would penetrate the outlet basin, making multiple grid cells occupy the same space. Again, the goal here is to maximize F_{GB} while maintaining acceptable values for $\underline{F}$ and $\sigma(\underline{F})$. Fig. 6 shows results of the study. Standard deviations for the individual forces are relatively uniform across all cases compared to the first study.

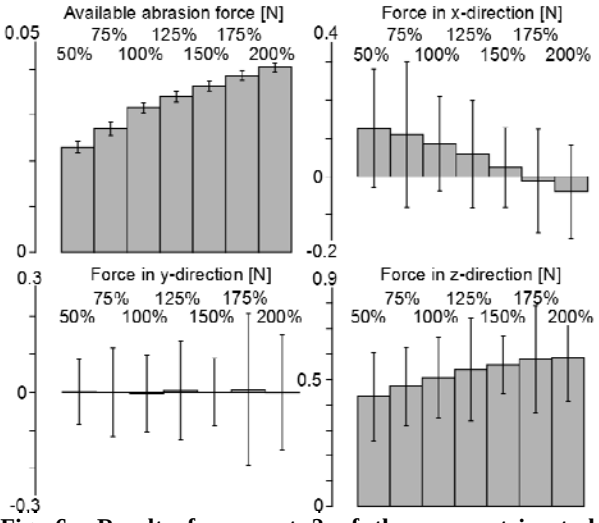

Fig. 6 Results from part 2 of the parametric study: abrasion force F_{GB} and exerted forces F_x, F_y, and F_z (error bars denote standard deviation).

Hence, the absolute values of the forces and how they compare across cases is the focus of this second study. It is easily seen that the abrasion force F_{GB} increases with higher offsets. This can be explained by the fact that the angle at flow's point of impact on the sphere between the flow's main direction and the surface of the sphere becomes larger as the offset increases. Greater viscous forces are a direct consequence of this. Although a maximum offset of 200% can not be exceeded, it is clear that there must exist an optimum offset beyond which abrasion force starts to drop. Should the angle mentioned before become perpendicular, viscous forces vanish, cancelling each other out as they are distributed uniformly in all directions. Inspecting the abrasion force in Fig. 6 supports this. Regarding F_{GB} as a function of offset h_o, there is a clear decrease in the slope of the function as offset increases. Assuming $F_{GB} \approx 0$ for $h_o = 23$ mm, the slope must become negative somewhere between $h_o = 2h_g$ and $h_o = 23$ mm. This can be further investigated in the future for different geometries that allow for higher offsets. Forces F_x in x-direction clearly display a reduction with increasing offset. Forces are minimal for $h_o = 1.5h_g$ and $h_o = 2h_g$. Forces F_y are similar across all cases while F_z shows increasing upward force with increasing offset. Forces F_z, nonetheless, only vary

between 0.43 N and 0.58 N. Based on this data, the optimal value for the offset is $h_o = 1.5h_g = 4.5$ mm. While only in third place for abrasion force, it delivers the lowest standard deviation across all directional forces F_x, F_y, and F_z. Furthermore, the force F_x is comparatively small. Hence, the sphere is subjected to the least amount of vibration with this setup, causing the magnetic bearing to emit less heat. Unfortunately, a tight manufacturing schedule did not permit for the second study to reach completion on time. Consequently, only results from the first parametric study could be considered which is why the following deals with a setup consisting of $h_g = 3$ mm, $h_d = 4$ mm, and $h_o = 3$ mm.

3.2 GrindBall Prototype

The optimum configuration determined previously is now simulated using a variety of rotation frequencies and mass flow rates (Table 2).

Forces F_x, F_y, and F_z as well as abrasion force F_{GB} are investigated. Finally, a relation is established which states the dependency of abrasion force F_{GB} on rotation frequency f and on standard volumetric flow rate $\dot{V}_N$. Note that $\dot{V}_N = \dot{m} / \rho_N$, where $\rho_N = 1.293$ kg·m^{-3} is the standard density of air at 273.15 K and atmospheric pressure. This representation is preferred over the mass flow rate as it is a more common quantification and is also the unit employed by the flow meter used in practice.

3.2.1 Pressure and Viscous Forces

Fig. 7 shows forces averaged over each constant flow rate with error bars denoting average standard deviation. While magnitudes of F_x are similar for all flow rates, their standard deviations increase severely with increasing $\dot{V}_N$. A similar observation can be made for F_z regarding standard deviation, however, magnitudes of F_z also increase with rising flow rate. Use of the tool is not impaired by upward force for high flow rates as even with max $(F_z + \sigma(F_z)) \approx 0.8$ N, the sphere still has 1.7 N of downward force resulting from its own weight at its disposal.

Table 2 Case configurations simulated for the prototype.

Flow rates	1	2	3	4	5
Frequencies	0	0	0	0	0
(Hz)	50	75	25	50	75
			100	100	150
Flow rates	6	7	8	9	10
Frequencies	0	0	0	0	0
(Hz)	50	50	50	50	200
	100	100	100	100	400
	200	250	300	350	

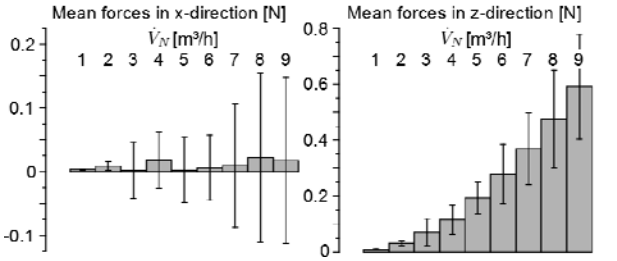

Fig. 7 Exerted mean forces F_x, F_y, and F_z averaged over constant volumetric flow rates.

3.2.2 Analysis of Available Abrasion Force

As seen in Fig. 8, abrasion force F_{GB} displays a linear dependency on rotation rate f for constant standard volumetric flow rates $\dot{V}_N^*$. This allows for a linear regression line to be fitted to each constant flow rate, which gives a mathematical approximation for the dependency of F_{GB} on f.

As is to be expected, the slope of each regression line is negative since the velocity gradients (and thus the viscous forces) between the sphere's surface and the flow impacting the sphere become lower as rotation frequency increases. The intercept of each regression line corresponds to the momentum transfer for a stationary sphere $F_{GB,0}$, i.e., the abrasion force for $f = 0$. Each null point can be interpreted as the idle rotation frequency f_0 for the corresponding flow rate due to the fact that if $F_{GB} = 0$, the sphere can neither accelerate nor decelerate. Fig. 9 shows $F_{GB,0}$ and f_0. To avoid dimensioned coefficients, the parameters F_{GB}, f, and $\dot{V}_N^*$ are made dimensionless using the radius of the sphere $r = 0.02$ m, the standard kinematic viscosity of air $\nu_N = 1.33 \times 10^{-5}$ m^2·s^{-1}, and the standard density of air $\rho_N = 1.293$ kg·m^{-3}. The resulting dimensionless variables are: $F^*_{GB} = F_{GB}/\nu_N^2\rho_N$, $f^* = f/\nu_N r^{-2}$ and

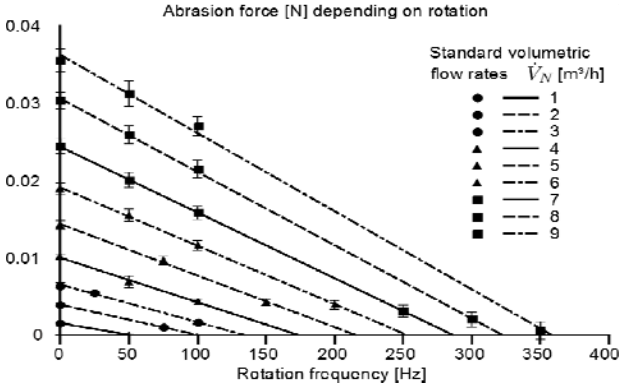

Fig. 8 Abrasion force with fitted regression curves for each standard volumetric flow rate.

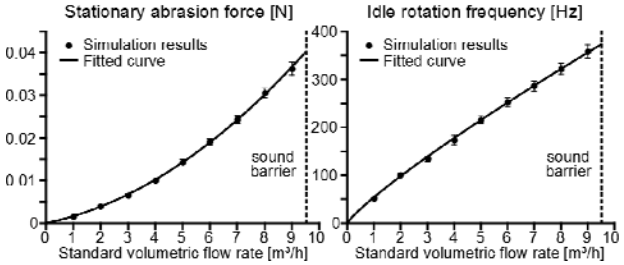

Fig. 9 Force transfers for a stationary sphere (left) and idle rotation frequency (right).

$\dot{V}_N^* = \dot{V}_N / \nu_N r$. A dimensionless relation for momentum transfer on to a stationary sphere is thus given by:

$$F_{GB,0}^* = 1.2198\dot{V}_N^{*2} + 5597.4383\dot{V}_N^* \quad (17)$$

A similar analysis can be done for idle rotation frequencies, which are extrapolated from the null points of the individual linear equations for constant standard volumetric flow rates:

$$f_0^* = 4.2086\dot{V}_N^{*6/7} \quad (18)$$

3.2.3 Abrasion Force Dependency

The relation between abrasion force F^*_{GB} and rotation frequency f^* is linear for constant volumetric flow rates. Furthermore, the 2D relations between $F^*_{GB,0}$ and $\dot{V}_N^*$ for $f^* = 0$ and between f_0^* and $\dot{V}_N^*$ for $F_{GB^*} = 0$ are known. A single equation relating all three variables to one another can hence be obtained using $F^*_{GB,0}$ as intercept, the ratio of $F^*_{GB,0}$ to f_0^* as the slope, and f^* as the dependant variable:

$$F_{GB}^* = F_{GB,0}^* - \frac{F_{GB,0}^*}{f_0^*} f = F_{GB,0}^* \left(1 - \frac{f^*}{f_0^*}\right) \quad (19)$$

Hence, available abrasion force F^*_{GB} is governed by:

$$F_{GB}^* = \left(1.22\dot{V}_N^{*2} + 5597\dot{V}_N^*\right)\left(1 - 0.24 f^* \dot{V}_N^{*\frac{6}{7}}\right) \quad (20)$$

Eq. (20) is of particular interest for the use of the GrindBall, as prior knowledge of the abrasion force and its behavior is required before commencing operation. Typically, particular materials require a certain amount of force. This required force could simply be plugged into Eq. (20), resulting in a 2D equation governing flow rate vs. rotation frequency. Thus, the flow rate can then be chosen to achieve a certain frequency for a given amount of force.

4. Conclusions

Having found a viable geometry and performed an extensive analysis of forces acting on the sphere, as well as having determined the force available for abrasion mathematically, the GrindBall is now ready for construction and subsequent operation. It remains to validate the results presented in this paper with experimental data. Examination of this first prototype shows that air is not a viable propulsion medium as the resulting abrasion force is simply too low for industrial use. Hence, a fluid with a high viscosity such as oil may prove to be a possible future alternative since it can transfer far more momentum through viscous stress. The next step of development is an 8 mm sphere which will build upon this first prototype and employ improvements inspired by the results presented here. Two supplemental ducts will be introduced vertically from the top in order to create enough downward force to enable the sphere to penetrate into a workpiece. Pneumatic propulsion will be replaced by hydraulic propulsion to increase momentum transfer. Also, the main duct will receive a larger offset pending a further parametric study with the new propulsion medium. Upon completion of the 8 mm GrindBall, further miniaturization will be performed, most likely beginning with 4 mm and then 2 mm. Should there still be room for further reduction, a 1 mm grinding sphere could also be developed. This gradual miniaturization process will not only aid in making the GrindBall

viable for industrial use, but also produce a unique and highly effective tool in the field of "micro-grinding". Hopefully this project will inspire others to develop new miniature tools and thus help the scientific community in finding new and innovative possibilities for machining small workpieces.

Acknowledgments

The authors wish to thank Carla Brandao (LFM) and Alexander Norbach (IALB) for their cooperation, and the North German Supercomputing Alliance (HLRN) for providing access to their computing facilities.

References

[1] E. Brinksmeier, C. Brandao, R. Gläbe, L. Schönemann, Micro grinding technologies, in: Proceedings of the 11th Euspen International Conference, Como, May 2011.

[2] E. Brinksmeier, R. Gläbe, C. Brandao, Achsenloses mikroschleifen, VDI-Z 9 (2012) 66-69.

[3] A. Norbach, Magnetic bearing for GrindBall, in: PCIM Proceedings, Nuremburg, Germany, 2012.

[4] A. Favre, Turbulence: Space-time statistical properties and behavior in supersonic flows, Physics of Fluids 26 (1983) 2851-2863.

[5] F.M. White, Viscous Fluid Flow, McGraw-Hill, USA, 1991.

[6] R.B. Montgomery, Viscosity and thermal conductivity of air and diffusivity of water vapor in air, Journal of Atmospheric Sciences 4 (1947) 193-196.

[7] C. Fureby, On subgrid scale modeling in large eddy simulations of compressible fluid flow, Physics of Fluids 8 (1996) 1301-1311.

[8] J.H. Ferzinger, M. Peric, Computational Methods for Fluid Dynamics, Springer Verlag, Germany, 1996.